



Deep learning-based segmentation, quantification and modeling of expansive soil cracks

Qi-cheng Hu¹ · Wei-min Ye^{1,2} · Wei-jian Pan¹ · Qiong Wang¹ · Yong-gui Chen¹

Received: 25 July 2022 / Accepted: 29 March 2023

© The Author(s), under exclusive licence to Springer-Verlag GmbH Germany, part of Springer Nature 2023

Abstract

Due to the periodic changes of climate, cracks are widely developed in expansive soils, leading to the destruction of soil integrity, the deterioration of physical strength, and eventually the instability of the expansive soil slope and other disasters. In this paper, a deep learning-based modeling method was proposed for soil crack networks characterization through steps of segmentation, quantification and simulation. Inspired by the U-Net convolutional neural network, a dilated convolution module was added to the backbone to enhance the crack segmentation capability and a subpixel edge detection algorithm was followed for accurate crack edge detection. Then, a deterministic or stochastic method was designed for crack network simulation. A case study of an expansive soil slope on the bank of Wadong Main Canal in the Pi-Shi-Hang Irrigation District, China, was conducted. Results show that the dilated U-Net model gained 0.24 and 0.25 improvement in *F1*-score and IoU (Intersection over Union) comparing to the conventional segmentation method (Otsu) and crack edge precision was further improved by 5.38%. The performances of proposed method including the image labeling, effect of crack thickness and environmental conditions, etc., are also explored. To validate the simulated crack network, crack areas at different depths were measured through X-ray images. Comparing with the simulation result, mean error rate of 1.05% was achieved. Thus, the proposed method can efficiently characterize soil crack networks using the field acquired crack images.

Keywords Convolutional neural network · Crack network · Deep learning · Expansive soil cracks · Model

1 Introduction

Expansive soil is a kind of high plastic clay and extremely sensitive to climate changes. During the cyclic wetting and drying processes, expansive soil periodically swells and shrinks, leading to generation of cracks and eventually formation of a complex cracks network system. This systematically cracks could be priority channels for liquid flow and pollutant transport [9, 13]. More importantly, cracks damage soil integrity and decrease soil strength, resulting in causing the instability of expansive soil slopes

and structures [19, 30, 40]. The development of cracks has been recognized as an important factor affecting the engineering safety in expansive soil areas. Especially in recent years, the frequently occurred extremely dry and wet climates in the world brings a severe crucible of the engineering design and operation safety in expansive soil areas. Therefore, it is extremely important to carry out quantitatively investigations on cracks and their development processes for expansive soils.

In this respect, to in-situ capture cracks is an important work. Early researchers mainly relied on manual observations with measurement tools such as sand filling [12], soil sectioning [26], etc., yet these methods could inevitably disturb the intact soil. Methods for fracture observations in rock mass were also applied in soil cracks investigations including scanline surveys [33] and window sampling [34], etc., which were labor-intensive. Other methods such as pouring liquid latex [31], dye tracing [29] were also employed to detect the preferential flow path in soil. But these methods were not suitable for measuring large

✉ Wei-min Ye
ye_tju@tongji.edu.cn

¹ Key Laboratory of Geotechnical and Underground Engineering of the Ministry of Education, Tongji University, Shanghai 200092, China

² United Research Center for Urban Environment and Sustainable Development, the Ministry of Education, Shanghai 200092, China

amount of field data and were susceptible to the natural conditions.

Fortunately, in recent years, digital imaging and artificial intelligence methods [6, 46] provide means for automatically capturing cracks and measuring fracture surfaces. For surface cracks, laser scanners with inbuilt cameras can both in-situ obtain images and point cloud data precisely and effectively [16]. For shallow internal cracks, indirect methods including electrical and electromagnetic methods [20], radar methods [24], computer tomography methods [38] and optical fiber methods [8], etc. are employed to detect apertures within soil body, although such methods are either expensive or inconvenient to operate on site.

To quantitatively identify cracks from the obtained images is another important issue for conducting quantitatively investigations on cracks. Image gray-scaling, image enhancement and image binarization were performed to reduce image complexity, suppress noises and segment cracks from background [2, 23, 32]. However, this kind of classic methods are often only applicable to high-quality images captured in the laboratory. To those obtained under field conditions, surface impurities, vegetation and shadows would greatly interfere the segmentation results. In the last few years, since convolutional neural networks (CNNs) have surpassed the recognition ability of the human eye on the ImageNet dataset [14], it is possible to train a deep learning model on field dataset to overcome these difficulties. In similar crack segmentation tasks, Huang et al. [18] used fully convolutional network (FCN) to extract both features of tunnel cracks and leakage defects with 0.8% error rate. More CNN models were proposed such as encoder-decoder-based method [4, 7], FCN-based method [27, 48], DeepLab-based method, [11] etc. These models were widely used in segmentations of concrete cracks, structure cracks and road cracks. Recently, Wang et al. [43] evaluated 5 different CNN models and pointed out that DeepLabv3 + with ResNet101 showed the best performance in detection of concrete cracks. To verify the efficiency of the CNN model in soil crack segmentation, Xu et al. [46, 47] compared the recognition performance of the deep learning model with that of the classic algorithm (Otsu) to show the robustness of the CNN model. For this purpose, they improved the model with Attention gate to tackle the uneven illumination situation. However, vegetation interference on the recognition performance still remains to be solved. In order to quantify cracks, i.e., calculate crack length, width and other parameters, skeletonization and vectorization of cracks were conducted to ensure that each crack was connected with single pixels in medial axis so as to record the pixel array and calculate corresponding geometric parameters [28, 37, 41]. However, this kind of calculation was based on the intact pixel of crack arrays, which would cause loss of precision. By

observing the edge pixels of cracks, it could be seen that the precise edge is located inside the pixel due to the hardware limitation of camera. Therefore, subpixel algorithm is needed to provide accurate parameters of crack network for subsequent modeling research.

To model the crack network, Horgan and Young [17] proposed a random walk method for simulating the development of cracks by assuming a constant crack width. In addition, researchers modeled the soil crack network with the method used in rock mass considering the similarity between them [10, 25]. However, the result obtained was quite different from the natural one. Vogel et al. [42] modeled dynamic crack formation based on a lattice of Hookean springs, yet the model parameters could not be deterministic easily through field images. In pursuing the geometric similarity between the generated crack network and a real one, Wang et al. [44] considered soil clods as polygons and used Voronoi diagram method to generate soil networks. The results showed that the generated network was similar as a uniformly cracked network and the model validity was verified by comparing measured and calculated permeability tensors. Other modeling methods such as smooth particle hydrodynamics (SPH) [3, 36] were also applied in the simulation of crack development, whereas such methods are not suitable for quick modeling base on crack geometry. Related works about deterministic crack network modeling, i.e., to model a crack network base on the exact crack geometry, were still lacking.

In fact, in engineering practice, identification, quantification and modeling of soil cracks should be implemented uniformly in a logical order. In this regard, a framework was established to combine the different processes. With the images captured, crack images were segmented, crack length, width, direction were calculated based on subpixel points, as well as crack networks were modelled using both the deterministic and stochastic methods. Finally, by assuming the linear relationship between crack surface width and depth, a 3D crack network model was established and validated based on the crack networks at different depths.

2 Development of the proposed method

2.1 Identification of cracks

2.1.1 U-Net structure

In order to establish the framework for identification, quantification and modeling of expansive soil cracks, the following procedures should be conducted and modified to adapt the cracks in expansive soil area. The first and foremost process is to identify the cracks from the complex

soil backgrounds. As the quantification and modeling procedures are based on the identification result, identification error would propagate through the whole process. Thus, a high accuracy method is essential and such method should also tolerate the impurities on the soil surfaces. In this regard, a deep learning segmentation model was introduced for its robustness in adaption of various environments [47]. The U-Net model is an image segmentation model proposed by Ronneberger and Fischer [35] and is widely used in segmentations of medical images such as cells and blood vessels. Considering the similarity of the blood vessels and expansive soil cracks, the U-Net structure was selected as the base structure of the model proposed in this work. As shown in Fig. 1, the U-shaped model can be decomposed into two parts: the encoder part (left) and the decoder part (right), where the left part learns crack features at different depths and the right part recovers details after pooling. The encoder receives the input RGB image with size of 572×572 , then passing through consecutive modules consist of convolution and down pooling layers, and an additional convolutional layer, to extract feature maps under different image sizes. Especially, the convolution operation was followed by batch normalization and ReLU activation by default in this structure. Each time the image passing the max pooling layer, its size gets halved. By symmetry, the decoder processes the output of encoder through consecutive modules as well with the pooling layers substituted for up-sampling layers that enlarge the image size. However, this kind of enlargement is lossy. To fill the loss, a skip connection is used to paste and crop the result of the corresponding level of encoder,

which gives the up-sampling layer additional details. In this way, the connection of different layers allows the network to obtain sophisticated features, including corners, shapes and some abstract features that humans cannot interpret, enabling more accurate image segmentation. Eventually, the model outputs 388×388 binary images where white pixels (value of 255) represented crack and black pixels (value of 0) were backgrounds. Note that the output size is smaller than the input one because of the convolution and down-pooling operations. To obtain the same image size, an overlap-tile strategy [35] was used by turning the input image into patches of size 388×388 and the missing data of $184 \times 184(572-388)$ was extrapolated by mirroring.

2.1.2 The dilated U-net

As mentioned above, crack images collected from the expansive soil areas often contain disturbances such as impurities, shadows, vegetations, etc., which make the expansive soil images more difficult to be identified than the medical images. Thus, the conventional U-Net model needed to be modified to enhance its identification capability. In the conventional U-Net model, pooling layers were used to reduce the image size so that the convolution window could receive more information (receptive field enlarged). However, by reducing the image size, image information also could be lost. In order to enlarge the receptive field, dilated convolution [5] was introduced to increase the window size of the convolutional layer (Fig. 2a), while still selected same number points (red points) as the conventional convolution to maintain the

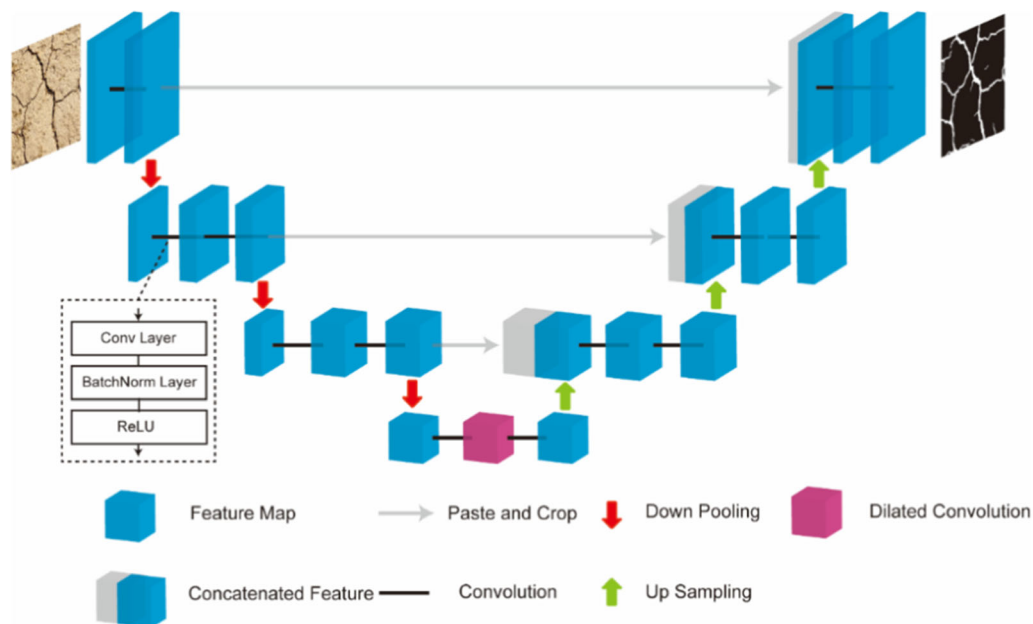


Fig. 1 The proposed dilated U-Net convolutional neural network

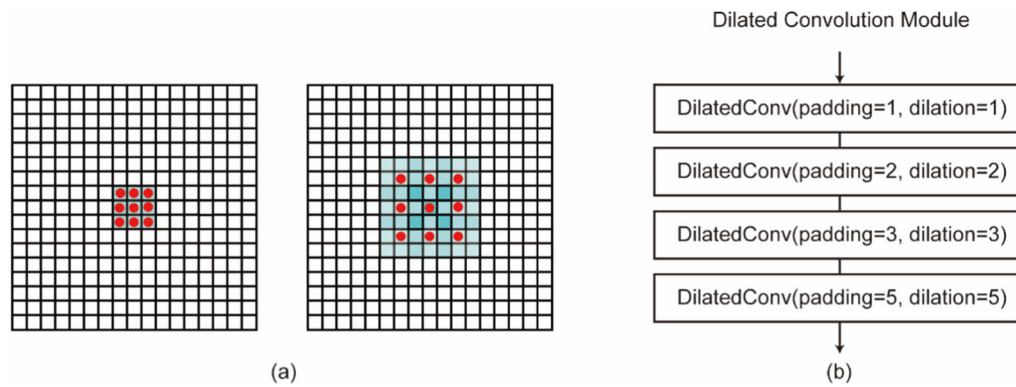


Fig. 2 Dilated convolution module. **a** Conventional convolution and dilated convolution diagram; **b** settings of dilated convolution module

computational complexity. Both parameters of *dilation* and *padding* were used to control the size and spacing of the window. The dilated convolution module (Fig. 2b) was added to the middle of the structure to maintain the symmetry of the model. As more image information could be learned, details such as edges and points could be recovered better theoretically.

2.1.3 Data labeling

Once the details of the deep learning model had been determined, the model was to be trained on the expansive soil crack dataset. To create the dataset, 350 crack images (cropped at size 572×572) (Fig. 3a) were collected from

the field. Each image contained one conspicuous crack network in the center. Especially, crack images were labeled manually (Fig. 3c), i.e., to color crack pixels in white (pixel value of 255) and background pixels in black (pixel value of 0) to provide ground truth images. This process was completed by creating an image mask to ‘fill’ the soil crack in the image (Fig. 3). Minor cracks comparing to the main crack network were deliberately not labeled as they were hard to distinguish from the contaminants on the soil surface. In addition, data augmentation operations such as random saturation (Fig. 3d), random colorization (Fig. 3e) and random flip (Fig. 3f) were applied to increase data variety.

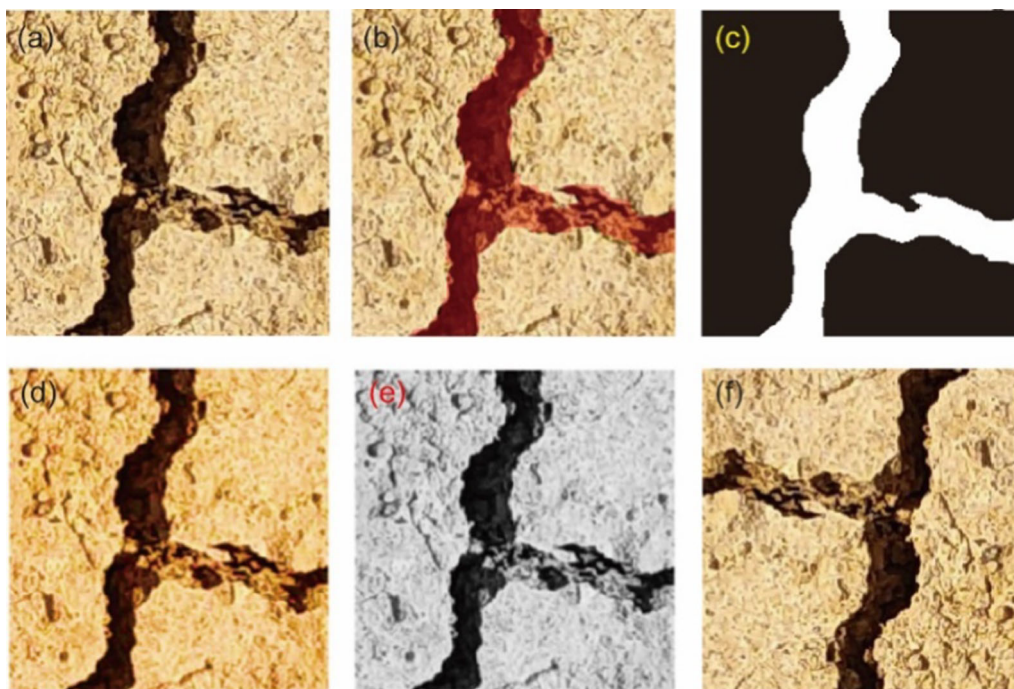


Fig. 3 Labeling image and data augmentation. **a** Soil crack image; **b** red mask; **c** Labeled image; **d** random saturation; **e** Random colorization; **f** random flip

2.1.4 Model training

As training a CNN model requires quite a number of labeled images, 350 expansive soil images processed in this work were not sufficient for training the CNN model proposed. In fact, labeling thousands of expansive soil crack images was time-consuming and costly. Fortunately, transfer learning has enabled the CNN model to learn with limited data by transferring knowledge from pre-trained weights on large datasets [45]. By applying the concept of transfer learning, the proposed model could be pretrained on a large dataset of soil crack related task firstly. Considering the good similarity between concrete cracks and expansive soil cracks, over 20,000 labeled concrete crack images were collected from open-source datasets in this work. To train the network, binary cross entropy (BCE) was selected to calculate the loss between binarized output image and ground truth image. It was represented as follows:

$$\begin{cases} l_n = -w_n[y_n \log x_n + (1 - y_n) \log(1 - x_n)] & n = 1, 2, \dots, N \\ L = \{l_1, l_2, \dots, l_N\} \end{cases} \quad (1)$$

where, N is the batch size, x_n and y_n are the n th output image and ground truth image, w_n is the n th weight. Therefore, the optimization goal was to minimize the loss function. This paper selected the commonly used deep learning optimization method Adam (Adaptive Moment Estimation) [22] as the model optimizer, which involved parameters such as learning rate, betas, etc. and the optimization process at time t was shown as follows:

$$\begin{cases} m_t = \beta_1 * m_{t-1} + (1 - \beta_1) * g_t \\ n_t = \beta_2 * n_{t-1} + (1 - \beta_2) * g_t^2 \\ \hat{m}_t = \frac{m_t}{1 - \beta_1^t} \\ \hat{n}_t = \frac{n_t}{1 - \beta_2^t} \\ \theta_t = \theta_{t-1} - \frac{\hat{m}_t}{\sqrt{\hat{n}_t} + \epsilon} * lr \end{cases} \quad (2)$$

where m_t and n_t calculates the moment estimation of first order and second order of gradient g_t , β_1 and β_2 are parameters called betas to smooth the addition, \hat{m}_t and \hat{n}_t are correction terms of m_t and n_t to make them as unbiased estimation, θ_t is the updating parameter, lr is learning rate and ϵ is a small number to avoid division of 0. In general, the learning rate was selected as 10^{-3} initially, and then it was set to gradually decay (halved) with the increase of every 1000 training iterations. Meanwhile, betas were set to 0.9 and 0.99, m_0 , n_0 were initialized as 0 and ϵ was set to 10^{-8} . These parameters were tuned according to the training loss curve.

The model was trained on NVIDIA RTX 3080 graphic card with 12 GB VRAMs, and the batch size was set to 8. The proportion of training set and test set was 60 and 20% of the whole dataset. The rest of the dataset were used to tune the parameters during the training process, that was, the validation set. By pre-training model on dataset of concrete cracks, pretrained weights of CNN model were obtained. Then, formal training (fine-tuning) could be conducted with soil crack dataset after loading the pre-trained weights (Fig. 4a). The training error curves of pre-training, training from scratch and formal training are shown in Fig. 4b. The results showed that the initial error and convergence time of formal training were halved comparing to training from scratch. After 200 epochs of training, model was tested on test set and the mean error of formal training and training from scratch were 0.09864 and 0.1355. This result was consistent with work of He et al. [15] as pre-training speeds up convergence early in training and increases accuracy slightly, but they also pointed out that pre-training did not necessarily improve final task accuracy.

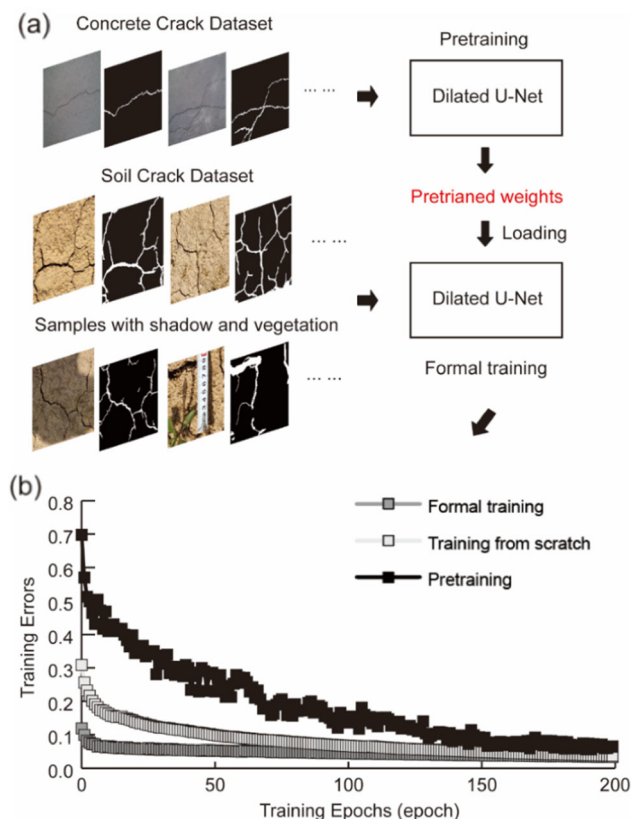


Fig. 4 Procedures of transfer learning. **a** Formal training of model loaded with pretrained weight; **b** training errors-epochs curve

2.1.5 Evaluation standard

In order to evaluate identification performance of the proposed model, different indicators were chosen and calculated. According to the confusion matrix (Table 1), the prediction results were divided into 4 circumstances including the True Positive (TP), False Positive (FP), False Negative (FN) and True Negative (TN). In this way, *Precision*, *Recall* rate, *F1-score*, *Accuracy* and *Intersection of Union (IoU)* were defined as follows:

$$\text{Precision} = \frac{\text{TP}}{\text{TP} + \text{FP}} \quad (3)$$

$$\text{Recall} = \frac{\text{TP}}{\text{TP} + \text{FN}} \quad (4)$$

$$\text{F1Score} = \frac{2 \times \text{Precision} \times \text{Recall}}{\text{Precision} + \text{Recall}} \quad (5)$$

$$\text{Accuracy} = \frac{\text{TP} + \text{TN}}{\text{TP} + \text{TN} + \text{FP} + \text{FN}} \quad (6)$$

$$\text{IoU} = \frac{|\text{TC} \cap \text{PC}|}{|\text{TC} \cup \text{PC}|} \quad (7)$$

where TC represents the True Class set, PC represents the Prediction Class set. These indexes assess the segmentation performance of models, whereas *Cost of Time* measures the running time of the model. Together, *F1 Score*, *Accuracy*, *IoU* and *Cost of Time* were chosen for the evaluation of models. The proposed model got 0.9596 on *accuracy*, 0.7716 on *F1-Score*, 0.6339 on *IoU* and 334,008,100 ns on average segmentation *cost time* of the test set.

2.2 Quantification of cracks

2.2.1 Separation of crack network

As the connecting part of the framework, the quantification step would either amplify or reduce errors based on the adopted methods. To minimize the errors, the pixel counting methods [25] of one pixel precision could be substituted for the sub-pixel precision methods. In this work, only crack width was calculated in sub-pixel precision to reduce overall computation cost since crack length array was not used in the following modeling of expansive soil cracks. Generally, soil crack quantification involves crack skeletonization, separation and calculation of length,

width, etc. Given that the crack network segmented by the proposed model was a whole (Fig. 5b), the information such as length and width of each individual crack could not be calculated directly. Therefore, it was necessary to complete the separation of the crack network, i.e., to extract the pixel array of each crack. Firstly, the skeletonization was carried out to ensure that cracks were only formed by connections of single pixels (Fig. 5c). In this regard, thinning algorithm proposed by Zhang and Suen [49] was applied by deleting pixels through iterations until the crack was connected by single pixels. On the basis of skeletonization, crack nodes (end nodes, intersection nodes and trunk nodes) were classified by the number of neighbor nodes to help separating each crack (Fig. 5a). Assuming an individual crack was consisted of several trunk nodes and two end or intersection nodes, crack arrays were recorded through iterations over the classified crack nodes and each crack array was given a color label (Fig. 5d).

2.2.2 Calculation of the crack length and width

With the crack arrays from the result of separation, the length of i th crack l_i was calculated at one pixel precision as the total number of corresponding array elements

$$l_i = |c_i|, \quad i = 1, 2, \dots, k \quad (8)$$

where $|\cdot|$ counts the number of the array elements, c_i is the i th pixel array, k is the total number of crack arrays. The crack width was measured conventionally by counting pixels around the medial axis [28], which assumed that the locations of the crack edges were determined by one pixel and such assumption would cause errors as Fig. 6a showed that the true edges (yellow curve) were inside one pixel. To search the precise locations of crack edges, accurate sub-pixel edge detection algorithm [39] was applied (Fig. 6b). The intensity of edge pixel (i, j) was defined as follows:

$$F_{ij} = \frac{AS_A + BS_B}{h^2} \quad (9)$$

where F , A , B are intensity values of edge pixel, area A and area B , S_A and S_B are the corresponding areas and h is the pixel size. Assuming crack edge was a straight line $y = a + bx$ inside a 5×3 moving window with center point (i, j) , the summation of pixel intensity under the line can be divided into three parts:

$$\begin{cases} \text{Sum}_L = \sum_{n=j-2}^{j+2} F_{i-1,n} = 5B + \frac{A-B}{h^2}L \\ \text{Sum}_M = \sum_{n=j-2}^{j+2} F_{i,n} = 5B + \frac{A-B}{h^2}M \\ \text{Sum}_R = \sum_{n=j-2}^{j+2} F_{i+1,n} = 5B + \frac{A-B}{h^2}R \end{cases} \quad (10)$$

where L , M , R are the corresponding areas which could be represented as follows:

Table 1 Confusion matrix of 2 classes

	True class 1	True class 0
Prediction Class 1	True positive	False positive
Prediction Class 0	False negative	True negative

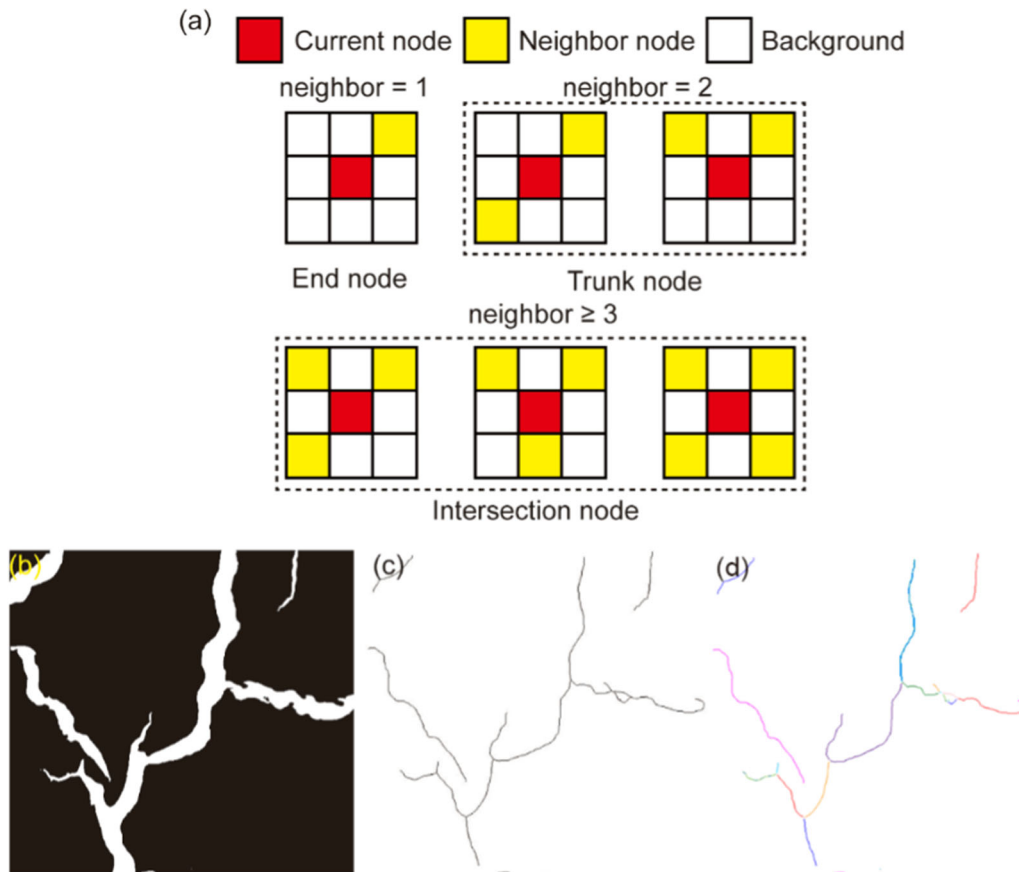


Fig. 5 Crack nodes and separation results. **a** Crack nodes; **b** segmentation result; **c** skeletonization result; **d** crack separation result

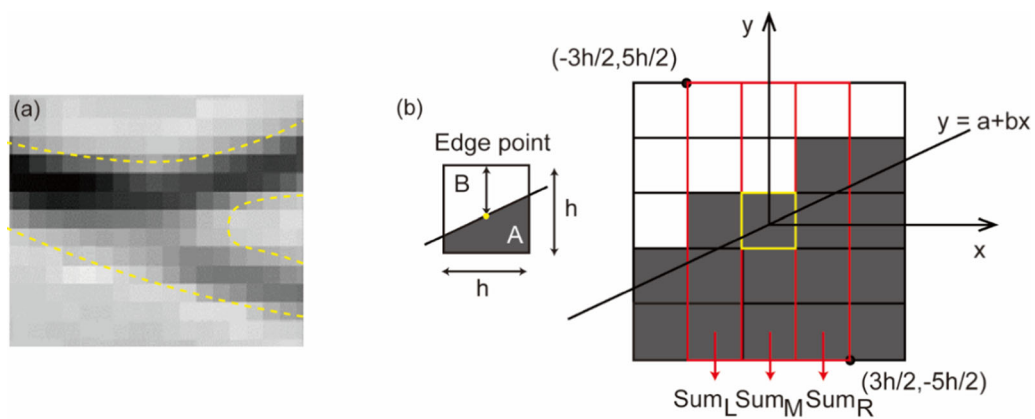


Fig. 6 Subpixel edge point searching



Fig. 7 Procedures of modeling the crack network. **a** Cropped field crack image; **b** diagram of crack network with dense nodes; **c** Diagram of crack model with sparse nodes and edges

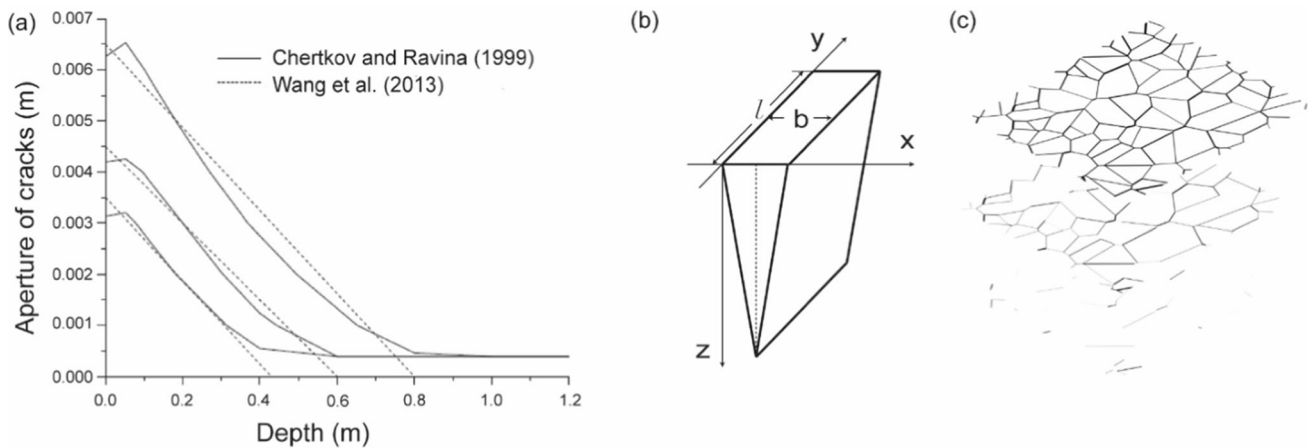


Fig. 8 Relation curve of aperture and depth. **a** Aperture-Depth curve; **b** V-shaped crack hypothesis

$$\begin{cases} L = \int_{-\frac{h}{2}}^{\frac{h}{2}} \left(a + bx + \frac{5h}{2} \right) dx = ah - bh^2 + \frac{5}{2}h^2 \\ M = \int_{-\frac{h}{2}}^{\frac{h}{2}} \left(a + bx + \frac{5h}{2} \right) dx = ah + \frac{5}{2}h^2 \\ R = \int_{\frac{h}{2}}^{\frac{3h}{2}} \left(a + bx + \frac{5h}{2} \right) dx = ah + bh^2 + \frac{5}{2}h^2 \end{cases} \quad (11)$$

Thus, coefficient parameters of edge line can be obtained as:

$$\begin{cases} a = \frac{2\text{Sum}_M - 5(A+B)}{2(A-B)}h \\ b = \frac{\text{Sum}_R - \text{Sum}_L}{2(A-B)} \end{cases} \quad (12)$$

where the intensity of A and B could be estimated using 3 pixels at corners and was shown as follows:

$$\begin{cases} A = \frac{1}{3}(F_{i,j+2} + F_{i+1,j+2} + F_{i+1,j+1}) \\ B = \frac{1}{3}(F_{i-1,j-1} + F_{i-1,j-2} + F_{i,j-2}) \end{cases} \quad (13)$$

Once coefficients of the edge line were solved, the edge point was calculated as the intersection point of the line and the middle axis of the edge pixel and width could be measured by 2 arrays of edge points of each crack.

It should be noted that these results were calculated in the unit of pixel. To cast pixels to meters, it was essential to calibrate the digital camera [50], obtaining the internal parameters, external parameters, and distortion coefficients of the chip, and then perform distortion correction on the captured image to determine the ratio between the pixels and the real world.

2.3 Crack network model

2.3.1 Graph model

In order to represent the surface geometry of expansive soil area, a crack network model was developed to simulate the natural soil surfaces based on results of identification and quantification. Stochastic methods could statistically represent the soil geometry, but natural cracks differ greatly in width and direction regionally such as tensile cracks and shearing cracks. In this regard, a deterministic modeling method was proposed based on graph to characterize crack differences. In the quantification period, crack nodes were scanned and saved as arrays. The crack network in Fig. 7a was scanned and presented in Fig. 7b, where the crack network could be considered as crack nodes connected with lines. Under this assumption, a *graph* could be used to describe such relationship between crack nodes. In the *graph*, crack nodes were defined as vertexes, and lines were defined as edges. Mathematically, it could be represented as follows:

$$\begin{cases} V = \{v_1, v_2, \dots, v_n\}, \quad n = 1, 2, \dots, m \\ E = \{(u, v) | u \in V, v \in V\} \\ G = (V, E) \end{cases} \quad (14)$$

where V is a vertex set, m is the number of vertexes, E is an edge set and G is a *graph*. In this way, a deterministic crack network could be modeled by a *graph* through setting vertex set as crack nodes and edge set as crack width. To simplify the dense *graph* model and reduce computational cost, only end nodes and intersection nodes were considered as vertexes (Fig. 7c). Then, a simplified crack model could be established.

However, deterministic modeling was not suitable for large area due to large sets of crack nodes and width arrays. Thus, Voronoi diagram method [1] was introduced to build

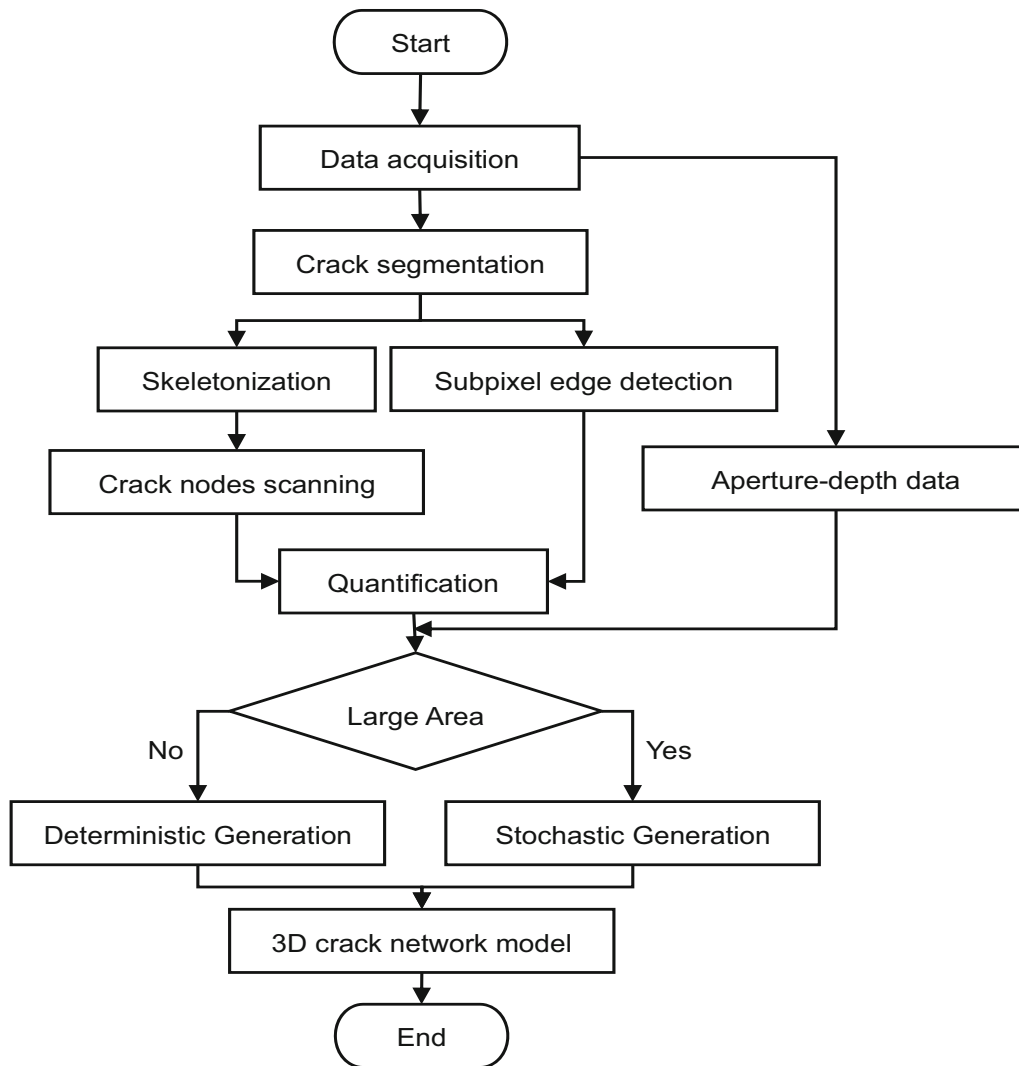


Fig. 9 Flowchart of a 3D crack network model using images

a uniformly distributed graph where only statistical values were needed to represent the large area. This method was a stochastic method, so crack geometries should keep consistent within the area. The positions of generated polygons were determined by seeds obeying a uniform distribution which was shown as follows:

$$\begin{cases} x_i = r_t(x_b - x_a) + x_a \\ y_i = r_t(y_b - y_a) + y_a \end{cases} \quad (15)$$

where x_a , x_b , y_a and y_b are size of generation area, r_t is a random number between 0 and 1. The crack width values of Voronoi diagram were sampled from fitted log-normal distribution and represented as follows:

$$\begin{cases} b_i = e^{(m+s\sqrt{-2\ln r_1}\cos 2\pi r_2)} r^3 < 0.5 \\ b_i = e^{(m+s\sqrt{-2\ln r_1}\sin 2\pi r_2)} r^3 \geq 0.5 \end{cases} \quad (16)$$

where r_1, r_2 and r_3 are all random numbers between 0 and 1, m is mean value and s is standard deviation value. This method could generate a uniformly distributed crack network based on density of soil clods in the area.

2.3.2 Crack networks inside the soil body

In order to identify crack networks inside the soil body, the shape of cracks needs to be assumed. Chertkov and Ravina [10] once proposed a relationship between aperture of a crack and its depth (Fig. 8a). Then, Wang et al. [44] used a linear line to simplify the relationship so that the crack could be assumed as V-shaped (Fig. 8b) and no rotation was considered. By fitting the aperture-depth line, crack networks at different depths could be generated either using a deterministic method or a stochastic method.

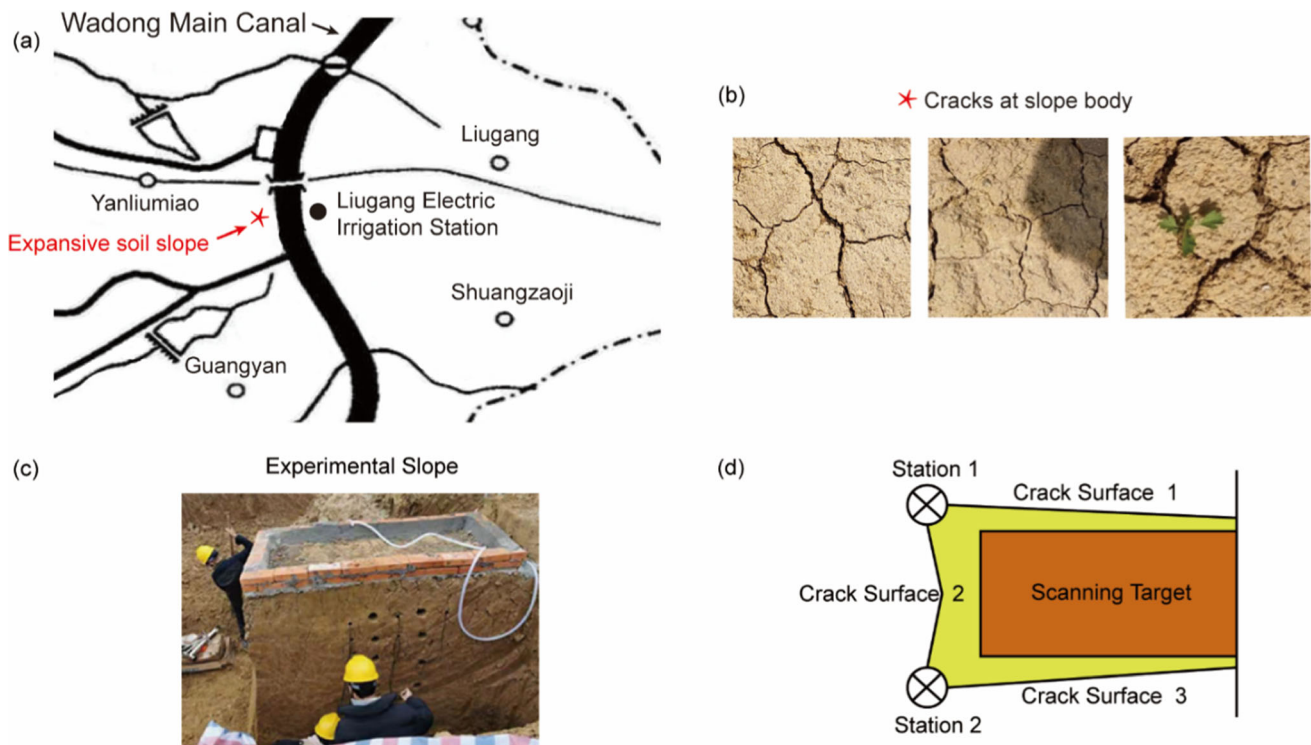


Fig. 10 Field data acquisition using a 3D laser scanner. **a** Map of the expansive soil slope; **b** cracks on the slope surface; **c** The test slope excavated; **d** scanning plan

Table 2 Basic physical Properties of the soil

Soil property	Values	
	CL	CH
Dry unit weight of soil (kN/m ³)	14.8	15.0
Specific gravity of soil particles	2.7	2.7
Liquid limit (%)	49.8	53.7
Plastic limit (%)	25.9	28.1
Free swelling ratio (%)	64.5	81.8

With surface crack width array W_s and slope of fitted line k , the i th crack width value at depth d could be calculated as follows:

$$w[i]_d = W_s[i] - k \times d \quad (17)$$

Based on these, a 3D crack network could be formed by synthesizing generated results along depth axis (Fig. 8c). The density of the 3D crack network was controlled by the generation gap along depth axis. In this way, given a field image and some width-depth data, a 3D crack network could be modeled (Fig. 9).

3 Case study

3.1 Site backgrounds

To validate the proposed framework, an expansive soil slope on the bank of the Wadong Main Canal (Fig. 10a), which opposites to the Liugang Electric Irrigation Station, in the Pi-Shi-Hang Irrigation District, China, was selected for the case study. The Pi-Shi-Hang Irrigation District is a famous large irrigation system with an irrigated area about 2 million acres. According to the site investigation report and related laboratory test results, this area is covered with wet yellow, brownish soil, which could be divided into 2 layers as types CL and CH according to the unified soil classification system (USCS) with differences in free swelling properties. The basic physical properties of the soil layers are shown in Table 2.

3.2 Cracks acquisition

To acquire images of surface cracks, a Leica P40 terrestrial laser scanner was employed to obtain both the image data and point cloud data in the field. Cracks at the slope body were captured under normal conditions, in shade and with vegetation (Fig. 10b). Meanwhile, to acquire development of vertical cracks in the soil, an experimental slope with 60 cm in width, 100 cm in length and 200 cm in height

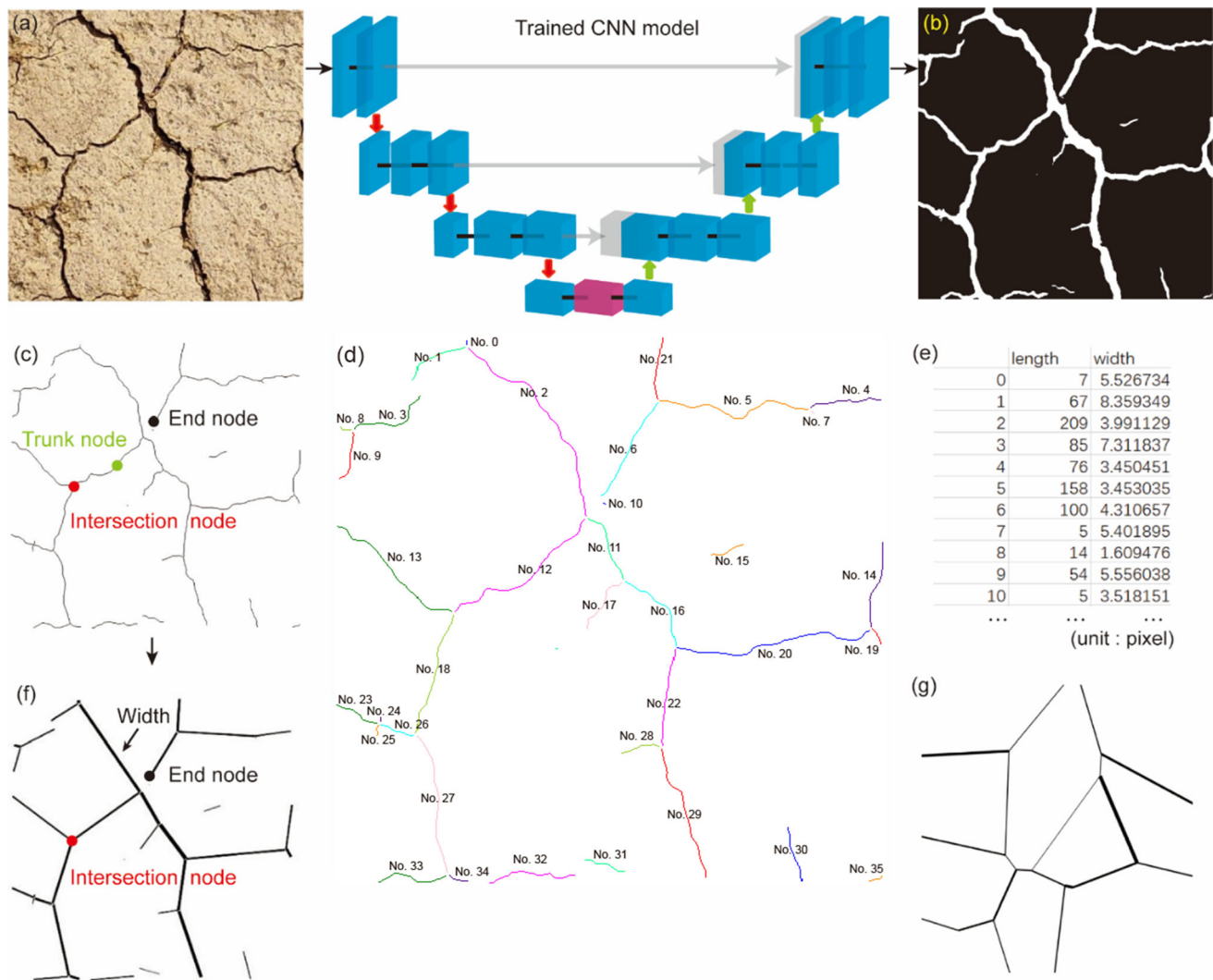


Fig. 11 Procedures of modeling surface crack networks. **a** Field crack image; **b** Segmented result; **c** skeletonization result; **d** separation result; **e** Part of length, width data. **f** Surface deterministic crack network model; **g** surface stochastic crack network model

with three faces empty was excavated (Fig. 10)). Then, the three empty faces of the experimental slope were scanned from two stations (Fig. 10d).

3.3 Segmentation, quantification and modeling of the field cracks

3.3.1 Segmentation of cracks

With the surface crack images captured under normal condition, in shade and with vegetations from the Pi-Shi-Hang Irrigation District, the dilated U-Net model was formally trained according to the training process shown in Fig. 4b. A test accuracy of 0.9596 was reached. By the trained CNN model, the crack image captured under normal condition (Fig. 11a) was segmented and the identification result was shown in Fig. 11b. The identification

result showed that the proposed method could greatly suppress noises caused by impurities, which could be commonly encountered in expansive soil areas due to the rough and dirty soil surface.

3.3.2 Quantification of cracks

For the segmented cracks in Fig. 11b, redundant pixels were reduced by the thinning algorithm and the crack skeleton was obtained (Fig. 11c). This skeleton was the abstraction of crack geometries without widths and it characterized the overall growth pattern of a crack network. To subtract the key points that could describe the growth pattern, the skeleton pixels were scanned and classified as end nodes, trunk nodes and intersection nodes. These nodes controlled the surface distribution of a crack network and were essential for the separation of cracks. To

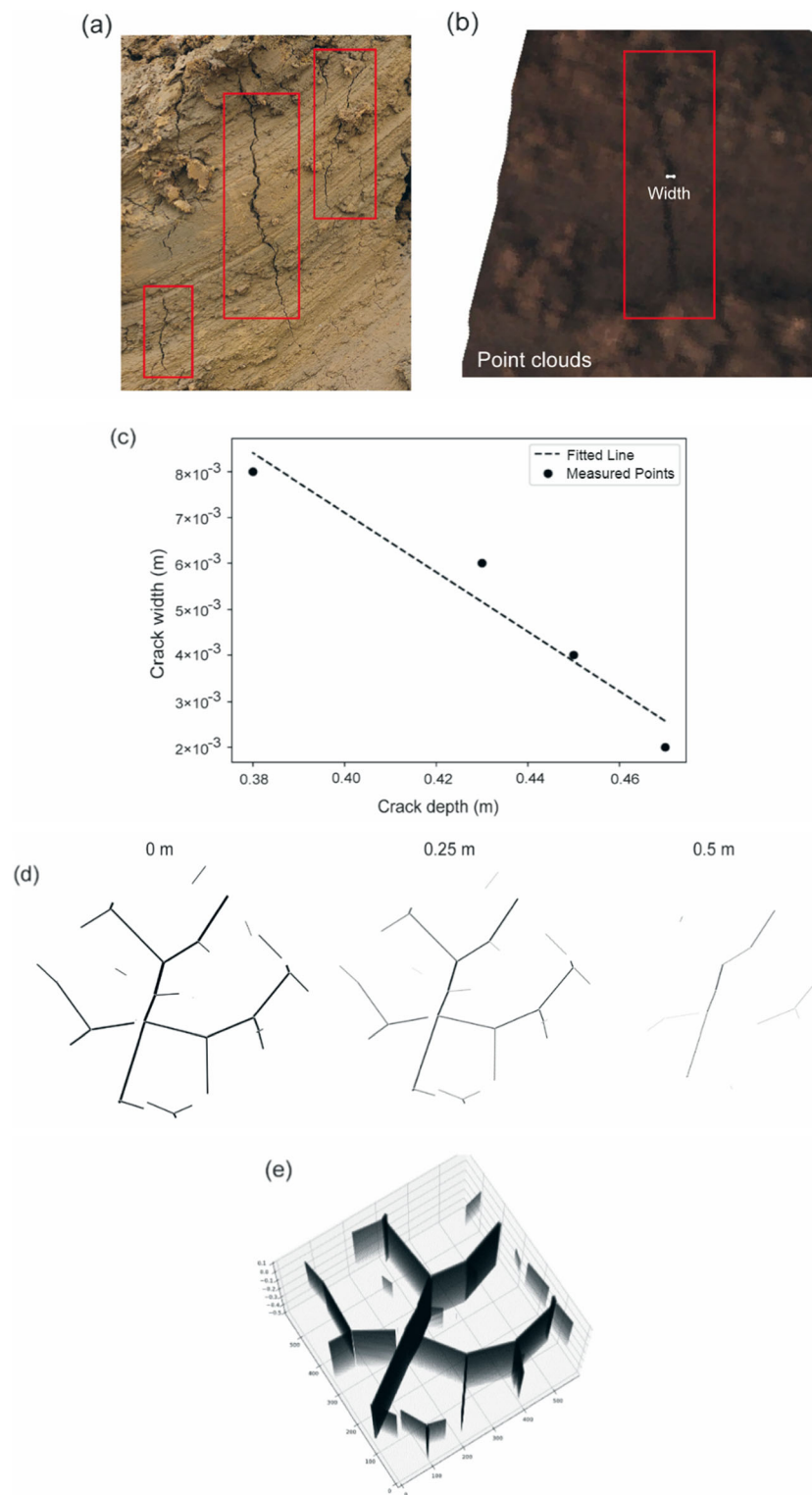


Fig. 12 Procedures of modeling 3D crack network. **a** Captured vertical cracks; **b** point clouds of a vertical crack; **c** fitted line of crack width and depth; **d** crack networks at depths of 0, 0.25 m, 0.5 m; **e** 3D crack network model

separate cracks, three node arrays were iterated to decompose the network into individual cracks and each crack was labeled in circulation of rainbow colors (Fig. 11d). With the separation results, crack length and width were calculated according to Eq. (8) and Eqs. (10–13). Part of the calculated results was shown in Fig. 11e, where the width was an average value of each crack. Finally, the width data was fitted in a log-normal distribution (Eq. 16) with a mean value of 1.638 and a variance of 0.651 in pixels.

3.3.3 Modeling of the surface cracks

Based on the quantification results of crack nodes in Fig. 11c and width results in Fig. 11e, parameters in Eq. (14) could be set to model the deterministic crack networks as a graph. In this regard, vertexes in Eq. (14) were set as end and intersection nodes in Fig. 11c and edges were set as mean widths of cracks in Fig. 11e. In this way, the deterministic crack network was shown in Fig. 11f. For the stochastic method, the soil crack network was assumed to be uniformly distributed. Thus, the soil crack network was modeled by using Eq. (15) to sample positions of soil clods (polygons) from a uniform distribution where the size of modeling area was set to be 0.5 m × 0.5 m. In addition, crack widths of each soil clod were sampled from the fitted log-normal distribution in quantification part. The result of stochastic crack network is shown in Fig. 11g. As a result, the deterministic one was closer to the real situation, however, it greatly relied on the binarized image, resulting in missing crack connectivity as the CNN model failed to segment the details. On the

contrary, stochastic result had no connectivity problem yet it only could show the global situation of the field as it was controlled by the statistical data of cracks.

3.3.4 Modeling of the vertical cracks

For the vertical cracks captured in the field (Fig. 12a), it could be seen that in the shallow part of soil, the linearity of crack width-depth relationship stood. Under such prerequisites, crack widths and depths were measured from the captured point clouds by calculating the distances between their spatial coordinates (x, y, z) (Fig. 12b) using commercial software Cyclone and fitted with a straight line ($k = 0.0648$) (Fig. 12c). In the measured data, tiny cracks with a width less than 0.001 m (after depth of 0.5 m) were not recorded due to the crack edge points were hardly distinguishable in the point clouds. Thus, the cracks were recognized as closed or were tiny cracks after the depth of 0.5 m. Then, according to Eq. (17) and slope of the fitted line, crack widths at different depths were calculated and the crack networks at depths of 0, 0.25 and 0.5 m were calculated in Fig. 12d. The crack network at 0.5 m shows that most of cracks were closed as expected, yet there were still few cracks existed due to their larger surface width in Fig. 11a. This indicated that fitted width-depth line was an overall declining trend in the excavated area. Eventually, a 3D crack network model was developed by synthesizing crack networks at different depths. As expected, the black color of cracks gradually transited to gray, then white, indicating the more closures of cracks (Fig. 12e).

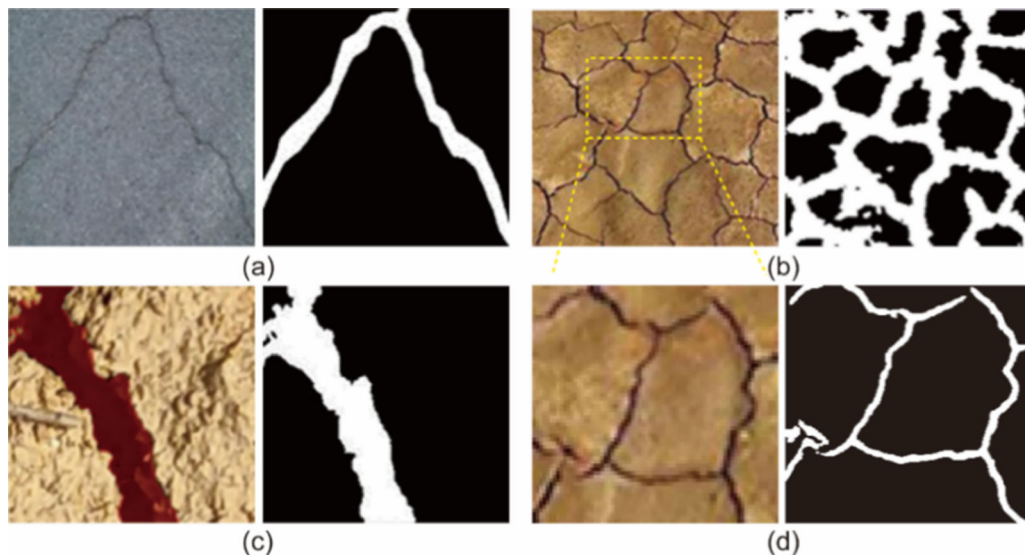


Fig. 13 Image labeling differences. **a** Thick 'covering' labeling; **b** segmentation result of training on thick labeled images; **c** Our labeling method; **d** segmentation result of training on filtered images

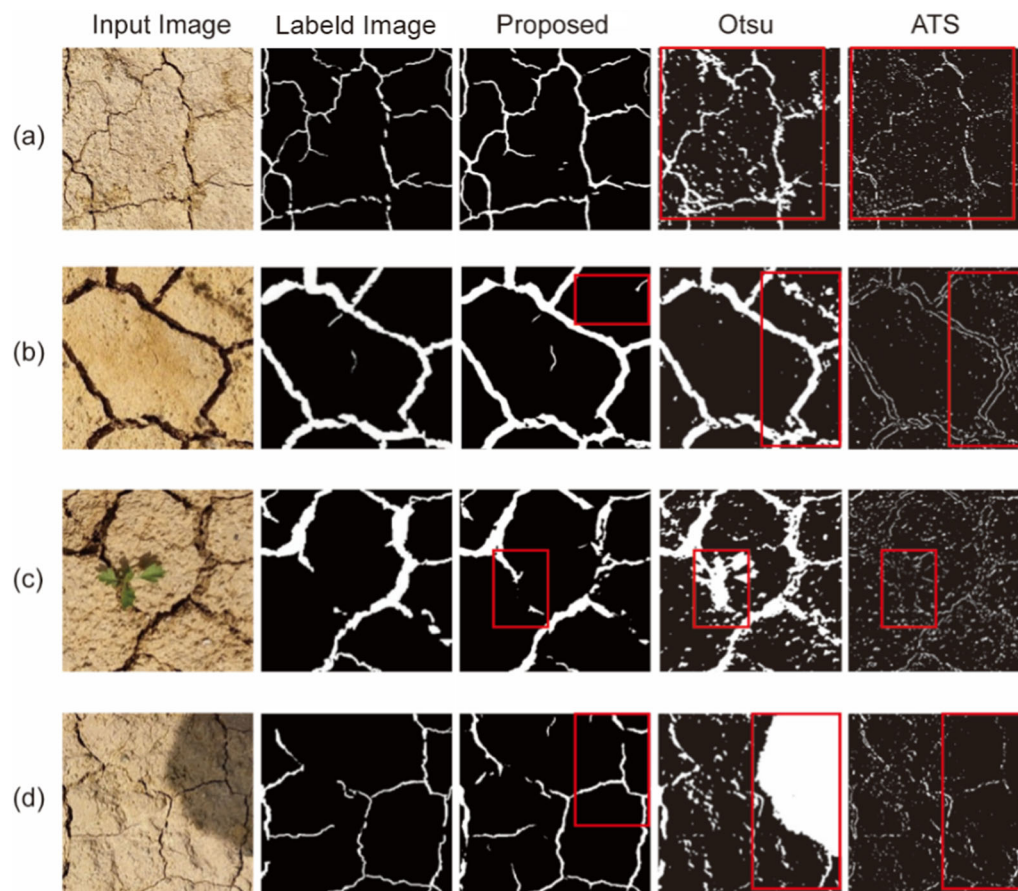


Fig. 14 Four different segmentation scenarios. **a** Thin crack network scenario; **b** thick crack network scenario; **c** crack network with plant; **d** crack network with shadow

Table 3 Performance of different models

Method	Accuracy	<i>F1</i> score	IoU	Cost time (ns)
Otsu	0.8507	0.5293	0.3928	997,750
Adaptive threshold method	0.8960	0.3031	0.1807	1,002,100
Proposed method	0.9595	0.7716	0.6339	334,008,100

4 Discussion

4.1 Image labeling

For open-source datasets, data screening was required due to their quality variations. A typical image sample in concrete crack datasets was presented in Fig. 13a, where the labeled crack was too ‘wide’ compared to the real crack. However, this kind of labeling accounted for a large proportion of the total samples, resulting in imprecise segmentation results (Fig. 13b). To refine the result, using ‘filling’ rather than ‘covering’ to label the entire crack

(Fig. 13c), in the meantime, deleting ‘wide’ labeled images to achieve fine segmentation results (Fig. 13d).

4.2 Effect of crack width and environmental conditions

Under the field conditions, crack size, shadows, vegetation and other factors will greatly influence segmentation performance. Therefore, it is always necessary to fully consider segmentation scenarios during soil crack dataset development. In this work, for the narrow cracks, wide cracks, vegetation interference and shadow interference scenarios considered, results obtained by the proposed method were compared to that by the Otsu Method, Adaptive Threshold (ATS) Methods in Fig. 14. Inputs to the proposed method were the original images, while the inputs to the Otsu and the ATS methods were gray-scale images after median filtering. Labeled images were manually made as truth images to quantify the errors. For the cracks without interferences of vegetation and shadows (Fig. 14a and b), the traditional algorithms could segment the whole crack network with noises depending on the

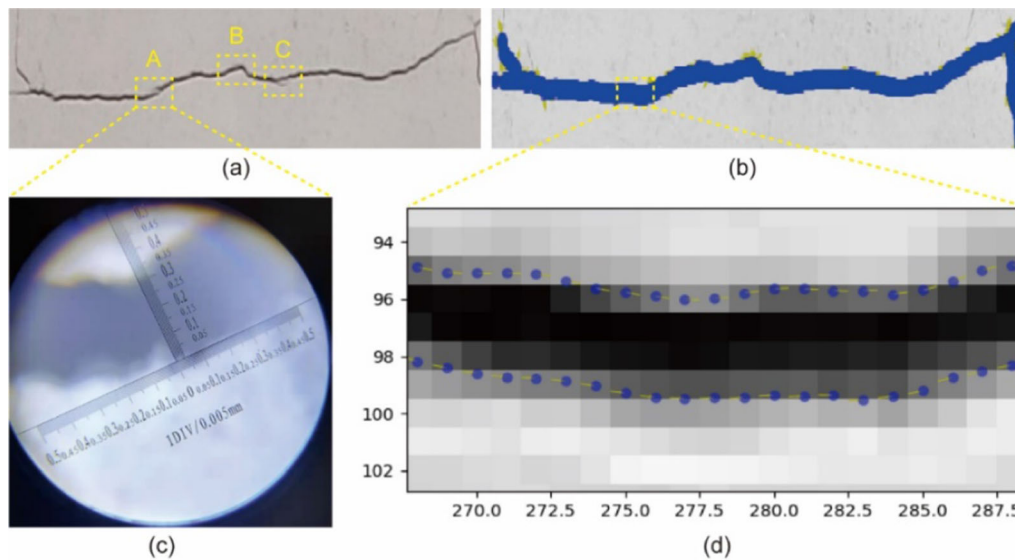


Fig. 15 Validation of crack subpixel width precision. **a** Input crack image; **b** Overall subpixel edge detection result; **c** view of area A under magnifier with ruler; **d** subpixel edge points of area A

Table 4 Comparison of different width calculation method

Area	True value (mm)	Subpixel calculation (mm)	Difference (mm)	Difference percentage (%)	Pixel Calculation (mm)	Difference (mm)	Difference percentage (%)
A	0.435	0.3942	0.0470	10.80	0.3461	0.0934	21.47
B	0.350	0.3166	0.0334	9.54	0.2596	0.0904	25.83
C	0.270	0.3132	0.0396	14.67	0.2596	0.0104	3.85
Mean value			0.0400	11.67		0.0647	17.05

Table 5 Properties of the expansive soil [21]

Soil property	Value
pH	7.52
Specific gravity, G	2.71
Atterberg limits	
Liquid limit (%)	78
Plastic limit (%)	27
Shrinkage limit (%)	9
Grain size distribution (%)	
Sand	3
Silt	15
Clay	82
Unified soil classification symbol	CH
Free swell index (%)	105
Standard Proctor compaction characteristics	
Maximum dry unit weight (kN/m ³)	13.15
Optimum moisture content (%)	28

roughness of the soil surface, while the proposed method in this work could restrain the noises caused by surface roughness. However, with interferences of vegetation and shadows (Fig. 14c and d), traditional algorithms were greatly affected, even failed to segment the cracks in the affected areas. The proposed model could distinguish the feature differences between vegetation, shadows and cracks, resulting in slightly influences on the segmentation results.

Performances of the three models are presented in Table 3. The best performance values are indicated in bold. Compared with that of the Otsu and ATS methods, the proposed method improved *Accuracy* by about 0.10 and 0.07, *F1-score* by 0.25 and 0.47, and the *IoU* by 0.24 and 0.45, although the *time cost* slightly increased with a cost about 0.33 s per image.

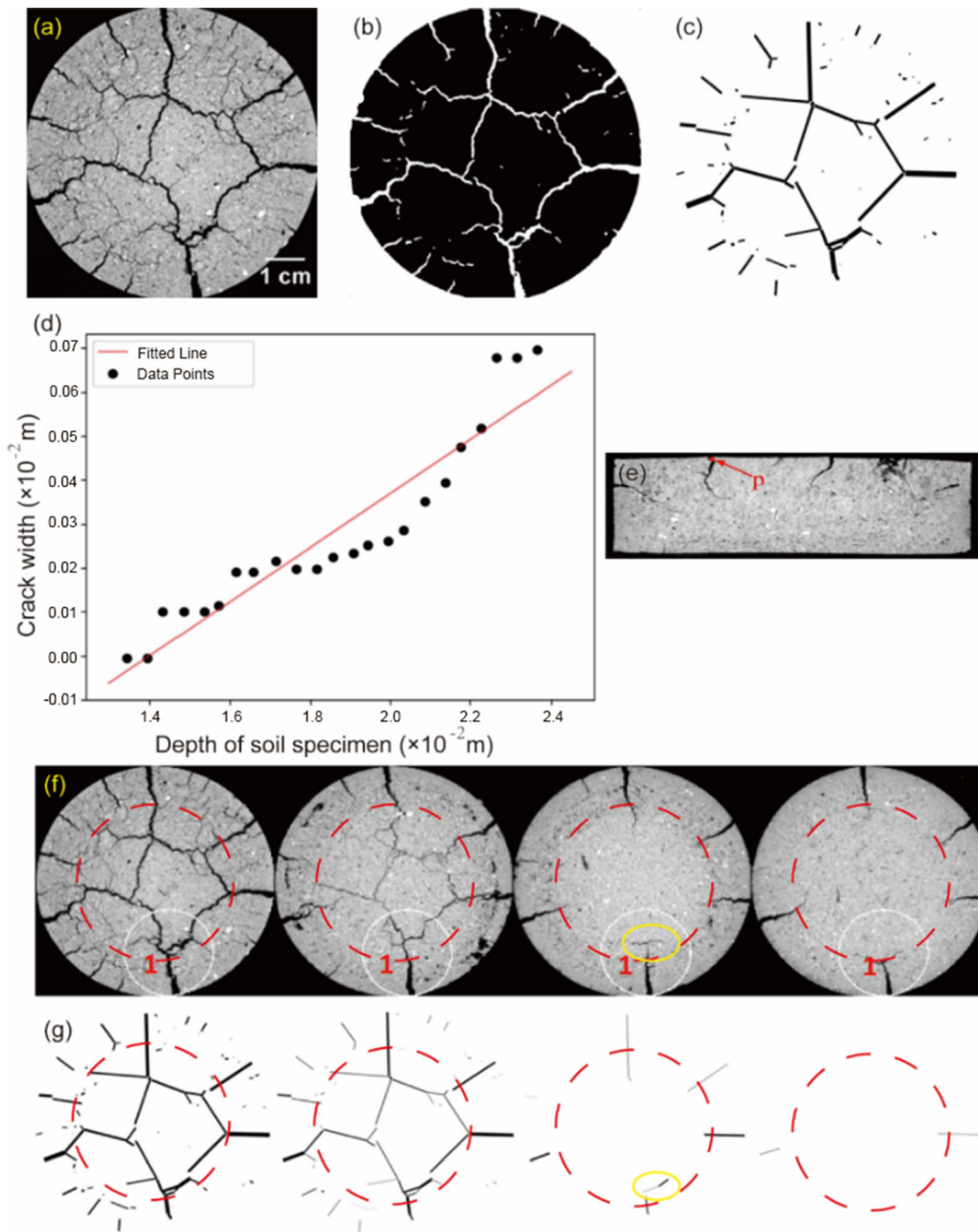


Fig. 16 Verification of generated networks at different depth with XCT images. **a** Crack surface XCT image; **b** binarized result of segmentation; **c** generated surface crack network; **d** fitting result of width-depth data of point p; **e** position of point p; **f** XCT images at depth of 5, 25, 50, 75%; **g** Generation results at corresponding depth

4.3 Validation of sub-pixel crack width calculation

To enhance precision of the crack width calculated, the subpixel edge detection algorithms offer a hardware cost-free method by determining edge location within a pixel. In Fig. 15a, 3 areas were randomly selected and measured using the magnifier with $DIV = 0.005 \text{ mm}$ (Fig. 15c) and a pixel ratio 0.1479 mm/pixel . Results of the subpixel edge points were shown in Fig. 15b and dots in Fig. 15d. By

recording both sides of subpixel edge points as arrays and searching the nearest edge point pair in the arrays, crack width at the current point was calculated. Comparing the subpixel results with the measured true values and pixel calculation values (Table 4) shows that subpixel calculation is 5.38% better than the pixel calculated. The smaller difference values and mean values are indicated in bold.

Table 6 Crack area ratio result

Percentage of soil specimen depth (%)	Crack ratio of XCT images (%)	Crack ratio of generated images (%)	Error rate (%)
5	5.38	4.33	1.05
25	2.83	2.01	0.82
50	1.88	0.77	1.11
75	1.39	0.17	1.22

4.4 Validation of the generated crack networks

The generation error could be evaluated by the geometric differences between the real crack networks and generated ones. To quantify this difference, a *crack area ratio* was defined as follows:

$$\text{crack area ratio} = \frac{\text{crack area}}{\text{surface area}} = \frac{\sum_i^m \text{width}[i] \times \text{length}[i]}{\text{surface area}} \quad (18)$$

where the *surface area* and *crack area* could be either measured by tools or calculated by width and length arrays. Since validating generated networks inside soil body was difficult, a series of XCT images obtained at different depths of a soil specimen was borrowed from Julina and Thyagaraj [21] at a water content of 38.5% (Fig. 15). Properties of the soil were listed in Table 5 and the soil specimen was 7.54×10^{-2} m in diameter and 3.0×10^{-2} m in height. In this case, the surface area and crack area of truth value are calculated with diameter of soil specimen and XCT crack scanning result, whereas crack area of the generated ones was calculated by arrays of width and length.

The surface XCT image was segmented by the model proposed in this work first. Then, the width and length of each crack were calculated and casted to meters with 1 cm flag in Fig. 16a. Based on the segmentation result (Fig. 16b), the surface crack network was generated using the deterministic generation method (Fig. 16c). In order to generate crack networks at different depths, width-depth data of point p was measured by XCT software and fitted with least squares method (Fig. 16d, e). As the slope of the fitted line was 0.06154, crack networks at depth of 5, 25, 50 and 75% were generated and compared with XCT images (Fig. 16f, g). Meanwhile, crack area ratio of both XCT images and generated ones were calculated and shown in Table 6. The results showed that cracks within the areas of dot circle were declining as expected, yet the non-propagating cracks near the edges caused the main difference in crack area ratio at depth of 50 and 75% and tiny cracks (fissures) that did not segmented by CNN model mainly

contributed to the error rate of crack area ratio at 5 and 25% depth. Changes of crack geometry in yellow circle caused minor differences as well. Overall, mean error rate of 1.05% was achieved and the generated crack networks could represent the geometric condition inside soil body.

5 Conclusion

In this paper, a deep learning-based modeling method of soil crack network was proposed based on three steps of crack identification, quantification and graph modeling. Meanwhile, the proposed method was validated in the case study of an expansive slope in Pi-Shi-Hang Irrigation District. Finally, related issues were discussed and conclusions were reached.

For crack identification, a dilated convolution module was added to recovered better edges and points and the trained dilated U-Net model achieved an accuracy of 96%. Meanwhile, in order to avoid errors generated by conventional quantification methods, an accurate subpixel edge detection algorithm was applied to search the precise locations of crack edges. With assuming of a linear relationship between width and depth of a crack, a deterministic method was proposed.

With an expansive slope selected, cracks obtained under four different scenarios of field conditions were segmented. Results showed that compared to that of conventional methods, the segmentation model proposed in this work exhibited better robustness in the field identification.

Using ‘filling’ rather than ‘covering’ to label the entire crack, fine labeled images were achieved. Comparing to the normal method, case studies showed that more accurate width values could be obtained using sub-pixel method. By modelling the XCT images of cracks using the deterministic crack network, the proposed method was validated even the modeling result was susceptible to the crack segmentation result that may cause network connectivity problem.

Acknowledgements This research was supported by the National Key R&D Program of China (2019YFC1509905).

Declaration

Conflict of interest The authors declare that they have no known competing financial interests or personal relationships that could have appeared to influence the work reported in this paper.

References

1. Aurenhammer F, Klein R (2000) Voronoi diagrams. In: Sack JR, Urrutia J (eds) Hand book of computational geometry, pp. 201–290. Elsevier, North Holland.

2. Baer JU, Kent TF, Anderson SH (2009) Image analysis and fractal geometry to characterize soil desiccation cracks. *Geoderma* 154(1–2):153–163
3. Bui HH, Nguyen GD, Kodikara J, Sanchez M (2015) Soil cracking modelling using the mesh-free SPH method. In: 12th Australia New Zealand Conference on Geomechanics (ANZ 2015).
4. Çelik F, König M (2022) A sigmoid-optimized encoder–decoder network for crack segmentation with copy-edit-paste transfer learning. *Comp-Aided Civil Infrastructure Eng* 37:1875–1890. <https://doi.org/10.1111/mice.12844>
5. Chen LC, Papandreou G, Kokkinos I, Murphy K, Yuille AL (2018) Deeplab: semantic image segmentation with deep convolutional nets, atrous convolution, and fully connected crfs. *IEEE Trans Pattern Anal Mach Intell* 40(4):834–848
6. Chen JY, Zhou ML, Huang HW, Zhang DM (2021) Automated extraction and evaluation of fracture trace maps from rock tunnel face images via deep learning. *Int J Rock Mech Mining Sci* 142(6):104745.
7. Chen J, He Y (2022) A novel U-shaped encoder–decoder network with attention mechanism for detection and evaluation of road cracks at pixel level. *Comp-Aided Civil Infrastructure Eng* 37:1721–1736. <https://doi.org/10.1111/mice.12826>
8. Cheng Q, Tang CS, Zhu C, Li K, Shi B (2020) Drying-induced soil shrinkage and desiccation cracking monitoring with distributed optical fiber sensing technique. *Bull Eng Geol Env* 79(8):3959–3970
9. Chertkov VY, Ravina I (2001) The effect of interaggregate capillary cracks on the hydraulic conductivity of swelling clay soils. *Water Resour Res* 37(5):1245–1256
10. Chertkov VY, Ravina I (1998) Modeling the crack network of swelling clay soils. *Soil Sci Soc Am J* 62(5):1162–1171
11. Choi W, Cha Y-J (2019) Sddnet: real-time crack segmentation. *IEEE Trans Industr Electron* 67(9):8016–8025
12. Dasog GS, Shashidhara GB (1993) Dimension and volume of cracks in a vertisol under different crop covers. *Soil Sci* 156(6):424–428
13. Flury M, Flühler H, Jury WA, Leuenberger J (1994) Susceptibility of soils to preferential flow of water: a field study. *Water Resour Res* 30(7):1945–1954
14. He K, Zhang X, Ren S, Sun J (2015) Delving deep into rectifiers: surpassing human-level performance on imagenet classification. *IEEE Computer Society, CVPR*
15. He K, Girshick R, Dollár P (2019) Rethinking imagenet pre-training. In: *Proceedings of the IEEE/CVF International Conference on Computer Vision*, pp 4918–4927.
16. Hirmas DR, Giménez D, Mome Filho EA, Patterson M, Drager K, Platt BF, Eck DV (2016) Quantifying soil structure and porosity using three-dimensional laser scanning. In *Digital soil morphometrics* (pp. 19–35). Springer, Cham.
17. Horgan GW, Young IM (2000) An empirical stochastic model for the geometry of two-dimensional crack growth in soil (with Discussion). *Geoderma* 96(4):263–276
18. Huang HW, Li QT, Zhang DM (2018) Deep learning based image recognition for crack and leakage defects of metro shield tunnel. *Tunn Undergr Space Technol* 77:166–176
19. Inoubli N, Raclot D, Moussa R, Habaieb H, Le Bissonnais Y (2016) Soil cracking effects on hydrological and erosive processes: a study case in Mediterranean cultivated vertisols. *Hydrol Process* 30(22):4154–4167
20. Jones G, Sentenac P, Zielinski M (2014) Desiccation cracking detection using 2-D and 3-D Electrical Resistivity Tomography: validation on a flood embankment. *J Appl Geophys* 106:196–211
21. Julina M, Thyagaraj T (2018) Quantification of desiccation cracks using x-ray tomography for tracing shrinkage path of compacted expansive soil. *Acta Geotech* 14:35–56
22. Kingma DP, Ba J (2014). Adam: a method for stochastic optimization. arXiv preprint, [arXiv:1412.6980](https://arxiv.org/abs/1412.6980).
23. Lakshmikantha MR, Prat PC, Ledesma A (2009) Image analysis for the quantification of a developing crack network on a drying soil. *Geotech Test J* 32(6):505–515
24. Levatti HU, Prat Catalán P, Ledesma Villalba A, Cuadrado Cabello A, Cordero Arias JA (2017) Experimental analysis of 3D cracking in drying soils using ground-penetrating radar. *Geotech Test J* 40(2):1–23
25. Li JH, Zhang LM, Wang Y, Fredlund DG (2009) Permeability tensor and representative elementary volume of saturated cracked soil. *Can Geotech J* 46(8):928–942
26. Lighthart TN, Peek G, Taber EJ (1993) A method for the three-dimensional mapping of earthworm burrow systems. *Geoderma* 57(1–2):129–141
27. Liu Y, Yao J, Lu X, Xie R, Li L (2019) Deepcrack: a deep hierarchical feature learning architecture for crack segmentation. *Neurocomputing* 338:139–153
28. Liu C, Tang CS, Shi B, Suo WB (2013) Automatic quantification of crack patterns by image processing. *Comput Geosci* 57:77–80
29. Lu JH, Wu LS (2003) Visualizing bromide and iodide water tracer in soil profiles by spray methods. *J Environ Qual* 32(1):363–367
30. Michalowski RL (2013) Stability assessment of slopes with cracks using limit analysis. *Can Geotech J* 50(10):1011–1021
31. Najm M, Jabro JD, Iversen WM, Mohtar RH, Evans RG (2010) New method for the characterization of three-dimensional preferential flow paths in the field. *Water Resources Res* 46(2).
32. Peng XH, Horn R, Peth S, Smucker A (2006) Quantification of soil shrinkage in 2D by digital image processing of soil surface. *Soil Tillage Res* 91(1–2):173–180
33. Priest SD, Hudson JA (1981) Estimation of discontinuity spacing and trace length using scanline surveys. *Int J Rock Mech Mining Sci Geomech Abstracts* 18(3):183–197
34. Priest SD (1993) *Discontinuity analysis for rock engineering*. Springer, Cham
35. Ronneberger O, Fischer P, Brox T (2015) U-net: convolutional networks for biomedical image segmentation. Springer, Cham
36. Sánchez M, Manzoli OL, Guimarães LJ (2014) Modeling 3-D desiccation soil crack networks using a mesh fragmentation technique. *Comput Geotech* 62:27–39
37. Shit PK, Bhunia GS, Maiti R (2015) Soil crack morphology analysis using image processing techniques. *Model Earth Syst Environ* 1(4):1–7
38. Taina IA, Heck RJ, Elliot TR (2008) Application of X-ray computed tomography to soil science: a literature review. *Can J Soil Sci* 88(1):1–19
39. Trujillo-Pino A, Krissian K, Alemán-Flores M, Santana-Cedrés D (2013) Accurate subpixel edge location based on partial area effect. *Image Vis Comput* 31(1):72–90
40. Utili S (2013) Investigation by limit analysis on the stability of slopes with cracks. *Geotechnique* 63(2):140–154
41. Vogel HJ, Hoffmann H, Roth K (2005) Studies of crack dynamics in clay soil: I. Experimental methods, results, and morphological quantification. *Geoderma* 125(3–4):203–211.
42. Vogel HJ, Hoffmann H, Leopold A, Roth K (2005) Studies of crack dynamics in clay soil: II. A physically based model for crack formation. *Geoderma* 125(3–4):213–223.
43. Wang JJ, Liu YF, Nie X, Mo YL (2022). Deep convolutional neural networks for semantic segmentation of cracks. *Struct Control Health Monit* 29(1):e2850. <https://doi.org/10.1002/stc.2850>
44. Wang Y, Di F, Charles WW, Ng. (2013) Modeling the 3D crack network and anisotropic permeability of saturated cracked soil. *Comput Geotech* 52(6):63–70

45. Wang K, Gao X, Zhao Y, Li X, Dou D, Xu C (2020) Pay Attention to Features, Transfer Learn Faster CNNs. ICLR.
46. Xu JJ, Zhang H, Tang CS, Cheng Q, Liu B, Shi B (2021) Automatic soil desiccation crack recognition using deep learning. *Geotechnique* 72(4):337–349
47. Xu JJ, Zhang H, Tang CS, Cheng Q, Tian BG, Liu B, Shi B (2022) Automatic soil crack recognition under uneven illumination condition with the application of artificial intelligence. *Eng Geol* 296:106495
48. Zhang A, Wang KC, Li B, Yang E, Dai X, Peng Y, Fei Y, Liu Y, Li JQ, Chen C (2017) Automated pixel-level pavement crack detection on 3d asphalt surfaces using a deep-learning network. *Comp-Aided Civil Infrastructure Eng* 32(10):805–819
49. Zhang TY, Suen CY (1984) A fast parallel algorithm for thinning digital patterns. *Commun ACM* 27(3):236–239
50. Zhang Z (2000) A flexible new technique for camera calibration. *IEEE Trans Pattern Anal Mach Intell* 22(11):1330–1334

Publisher's Note Springer Nature remains neutral with regard to jurisdictional claims in published maps and institutional affiliations.

Springer Nature or its licensor (e.g. a society or other partner) holds exclusive rights to this article under a publishing agreement with the author(s) or other rightsholder(s); author self-archiving of the accepted manuscript version of this article is solely governed by the terms of such publishing agreement and applicable law.